



# Design and qualification of a recessed satellite cornercube retroreflector for ground-based attitude verification via satellite laser ranging

Nils Bartels<sup>1</sup> · Paul Allenspacher<sup>1</sup> · Sven Bauer<sup>2</sup> · Benjamin Rödiger<sup>3</sup> · Fabian Sproll<sup>1</sup> · Wolfgang Riede<sup>1</sup>

Received: 28 November 2018 / Revised: 15 March 2019 / Accepted: 16 May 2019 / Published online: 21 June 2019  
© The Author(s) 2019

## Abstract

The design and qualification of a retroreflector specifically designed for a CubeSat (CUBEL) is described. The CubeSat will be launched to space in 2019 and demonstrate the latest generation of the optical space infrared downlink system developed by the German Aerospace Center together with the industrial partner Tesat-Spacecom. The retroreflector is optimized to allow for a coarse verification of the satellites attitude control system. By analyzing the returning photon count during satellite laser ranging (SLR) when the satellite is operated in station pointing mode attitude information is obtained. To achieve this goal, the entrance face of the retroreflector is recessed by a circular tube-shaped aperture. Due to this recession, the signal reflected from the retroreflector falls off rapidly when the retroreflector is tilted away from the SLR station. From measurements of the retroreflectors far-field diffraction pattern and calculations, we believe that it should be possible to determine the orientation accuracy of the satellite to within  $\pm 2^\circ$ . The proposed method is an effective and cheap way for coarse attitude control, e.g., for satellites of mega-constellations with any existing satellite laser ranging ground station.

**Keywords** Retroreflector · Attitude control · CubeSat · OSIRIS · Laser communication

## 1 Introduction

The German Aerospace Center (DLR) is working on the development of compact laser communication payloads for low-earth orbit (LEO) satellites [1]. Within the optical space infrared downlink system (OSIRIS) program two prototypes (OSIRISv1 on Flying Laptop [2] and OSIRISv2 on BiROS) of laser communication terminals have been tested on Earth observation satellites. A third generation (OSIRISv3) with a strongly increased rate of data transfer (up to 10 Gbit/s) is

foreseen on the Bartolomeo platform (Airbus) onboard the International Space Station in 2019.

In parallel to this development line targeting for high data rates, a miniaturized OSIRIS version called OSIRIS-4CubeSat [1] is under development, which is planned to be launched to space on the 3U CubeSat CUBEL in spring 2019. The goal of this mission is to demonstrate a downlink data rate of 100 Mbit/s under the restrictions (size, power consumption and weight) imposed by the CubeSat technology. To access the growing CubeSat market, the system is based on commercial of the shelf (COTS) technology, uses 8 W of electrical power only and is integrated in a compact design (0.3 U) of low mass (350 g).

A major technological challenge in optical downlink laser communication is that the data transmitting laser on the satellite needs to be pointing accurately towards the receiving ground station during data transfer. The required precision depends on the divergence of the laser used for data transfer, which is in the order of 200  $\mu$ rad with OSIRISv2. To achieve this goal, OSIRIS4CubeSat will use a combination of body pointing and active beam steering. The goal of the satellites attitude control system (ACS) is to provide a pointing accuracy of  $\pm 1^\circ$ , and the remaining accuracy comes from a fine pointing unit integrated

✉ Nils Bartels  
nils.bartels@dlr.de

<sup>1</sup> Deutsches Zentrum für Luft- und Raumfahrt (DLR),  
Institut für Technische Physik, Pfaffenwaldring 38-40,  
70569 Stuttgart, Germany

<sup>2</sup> Helmholtz-Zentrum Potsdam, Deutsches  
Geoforschungszentrum, Telegrafenberg, 14473 Potsdam,  
Germany

<sup>3</sup> Deutsches Zentrum für Luft- und Raumfahrt (DLR),  
Institut für Kommunikation und Navigation, Satellitennetze,  
Münchner Straße 20, Oberpfaffenhofen, 82234 Wessling,  
Germany

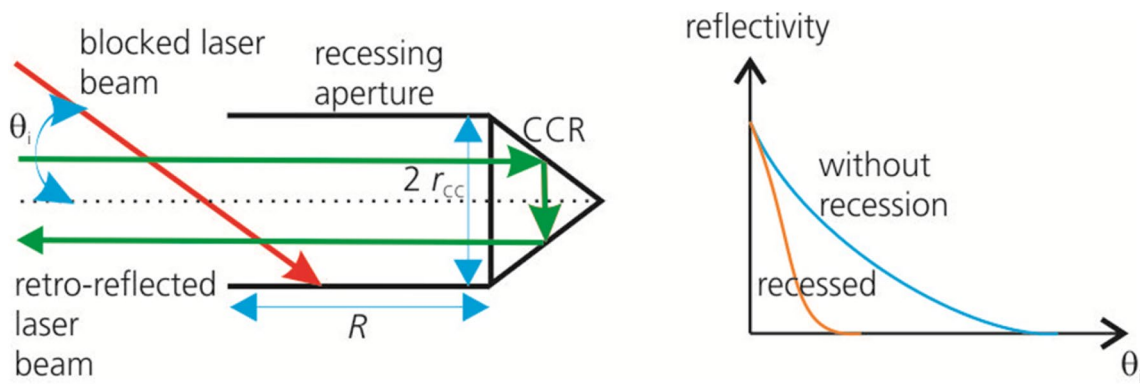


**Fig. 1** Concept of a recessed retroreflector and the effect of the angular dependence on the reflectivity. Left: a CCR with an entrance face of diameter of  $2r_{cc}$  is recessed by an aperture of length  $R$ . This leads to a shielding of incoming laser radiation at high incidence angles  $\theta_i$ .

Right: Reflectivity of recessed and unrecessed retroreflectors when illuminated by a large laser beam with a homogeneous intensity distribution

in OSIRIS4CubeSat. The control of this fine pointing unit is based on a tracking algorithm that scans for the ground station beacon laser (which is simultaneously the uplink laser) and tracks the ground station during the overflight.

A prerequisite for the functioning of this closed-loop optical tracking system is that the ACS is properly working and allows for a station pointing mode to within  $\pm 1^\circ$ . To independently verify this pointing accuracy, the CUBEL satellite features a specially designed cubed corner retroreflector (CCR). The CCR is equipped with an additional field stop. This is achieved by placing the CCR inside a circular tube (holder) which shields the entrance face of the CCR from laser radiation coming at high-incidence angles (see Fig. 1). Thus, we reduce the field of view (FOV) from  $\pm 20^\circ$  (FWHM) to  $\pm 5^\circ$  (FWHM). Of course, the FOV could be chosen even smaller by increasing the length of the circular tube.

The concept of using recessed retroreflectors has been used previously, e.g., on WESTPAC (NORAD ID 25398) and GFZ-1. Following this work, we describe the design and testing of the recessed retroreflector for the CUBEL satellite. Furthermore, we discuss the feasibility of attitude verification in an experiment with the SLR ranging station (Uhlandshöhe Research Observatory of the DLR in Stuttgart, Germany) [3, 4].

## 2 Layout of the recessed retroreflector

Figure 2 shows the layout of the recessed retroreflector assembly. The central part of the design is a commercially available retroreflector (Edmund Optics #45-202) with a diameter of 12.7 mm. Technical details on the CCR are summarized in Table 1. We tested the far-field diffraction pattern (FFDP) of eight of these retroreflectors and selected one with a symmetrical FFDP for use in the flight module

(see Appendix B for details). We decided to use a silver coated retroreflector as this allows for SLR at different laser wavelengths, which does not impose a wavelength requirement on SLR stations (as opposed to a CCR with a single wavelength dielectric coating).

The assembly will be attached to the wall of the CUBEL satellite close to the star tracker, pointing in the same direction as OSIRIS4CubeSat. The CCR is clamped between a mount and a retaining ring. The retaining ring does not only hold the retroreflector into place but also shadows the CCR's front face at oblique angles of incidence. The length of the shadowing cavity is  $R = 14$  mm and has a diameter of  $2r_{cc} = 10$  mm (see panel b of Fig. 2).

Both the mount and the retaining ring are made from titanium<sup>1</sup> and can be screwed together. To secure that this connection cannot loosen up due to vibrations, the assembly was additionally glued using space-qualified adhesives (Norland Products Inc., NOA 81 and MAP, MAPSIL QS 1123). The recessed retroreflector was assembled in a clean-room environment at DLR in Stuttgart. A qualification model of the assembly was vibration tested at DLR Bremen.

To obtain a small FOV (which requires a long recessing tube in front of the CCR) while at the same time maintaining a sufficient photon count in SLR (see Sect. 4), the CCR holder is partly placed within the satellite structure. The holder is attached to the satellite wall via three screws (see panel d of Fig. 2). This way, the holder only sticks out of the satellite by 12 mm and fits into the orbital CubeSat deployer (the CubeSat is ejected via a spring mechanism).

<sup>1</sup> Titanium was chosen because of its light weight and because the linear thermal expansion coefficient at room temperature of  $\alpha(\text{Ti}) = 8.6 \times 10^{-6}/\text{K}$  closely matches the thermal expansion of N-BK7 of  $\alpha(\text{N-BK7}) = 7.1 \times 10^{-6}/\text{K}$ .

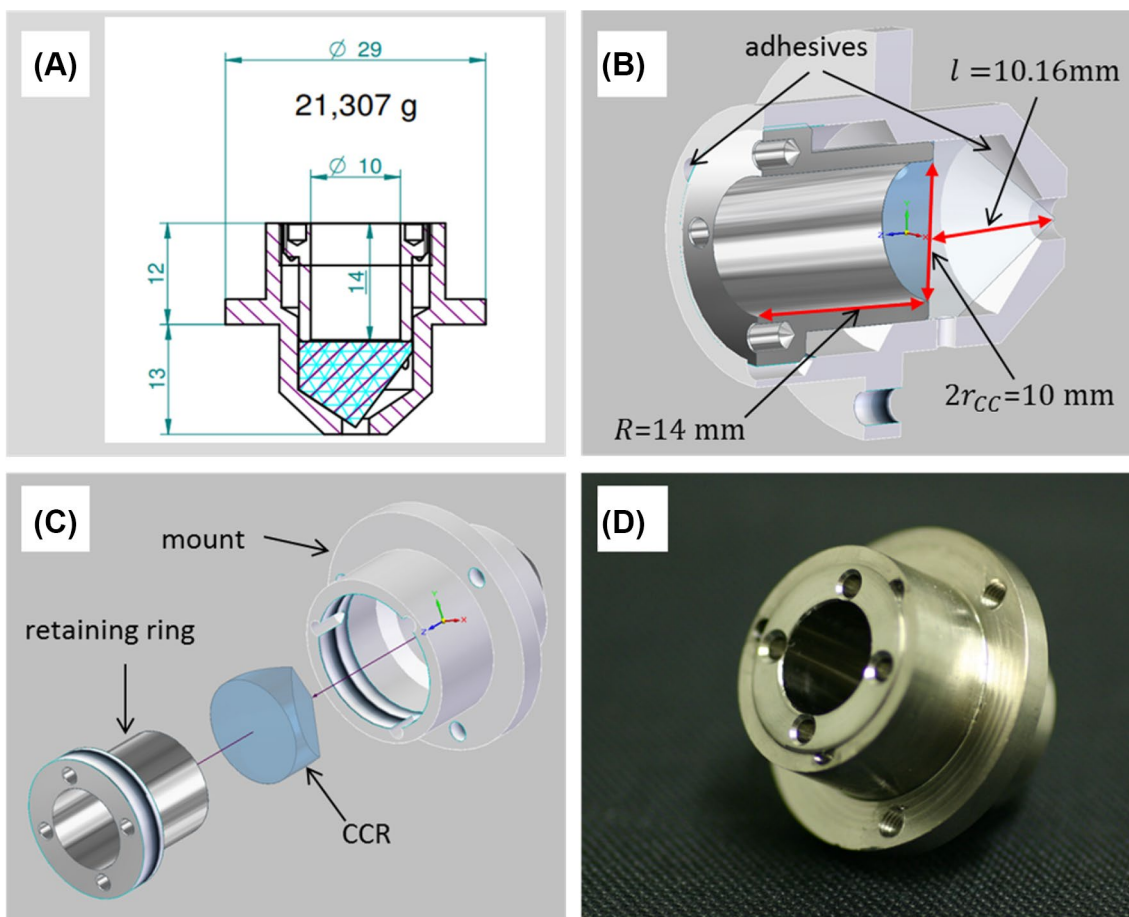


**Fig. 2** Design of the recessed retroreflector. **a, b** Sectional views and contain information on the dimensions (all given in the unit of mm). **c** A sectional view of the design and **d** a photo of the finished assembly

**Table 1** Specifications of the retroreflector

Specifications of the retroreflector	
Manufacturer	Edmund optics #45-202
Diameter	12.7 mm
Substrate	N-BK7
Coating	Front facet: uncoated Back facets: protected Ag
Height (= <i>l</i> )	10.16 mm
Surface accuracy	$\lambda/8$
Beam-angle tolerance	5 arcsec

### 3 Retroreflector characterization

The mathematics for calculating the optical cross section of retroreflectors and retroreflector-arrays has been greatly advanced by Arnold [5].

#### 3.1 SLR geometry

Throughout this article, we will use the same mathematical symbols as introduced by Stephenson [6], see Fig. 3. For most

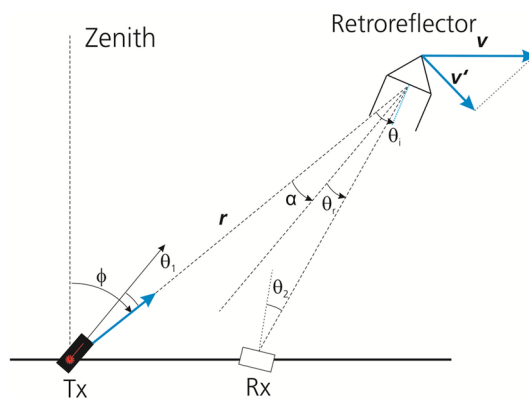


**Fig. 3** Diagram illustrating the angles defined for the satellite laser ranging geometry. For generality, the transmitter (Tx) and receiver are shown in separate positions, but are collocated in our and most other SLR experiments. However, the velocity component  $v'$  of the satellite (normal to the position vector  $r$ ) leads to a rotation of the reflected beam by the angle  $\theta_r = \alpha$ , where  $\alpha$  is the velocity aberration. The figure is adapted from Ref. [6]

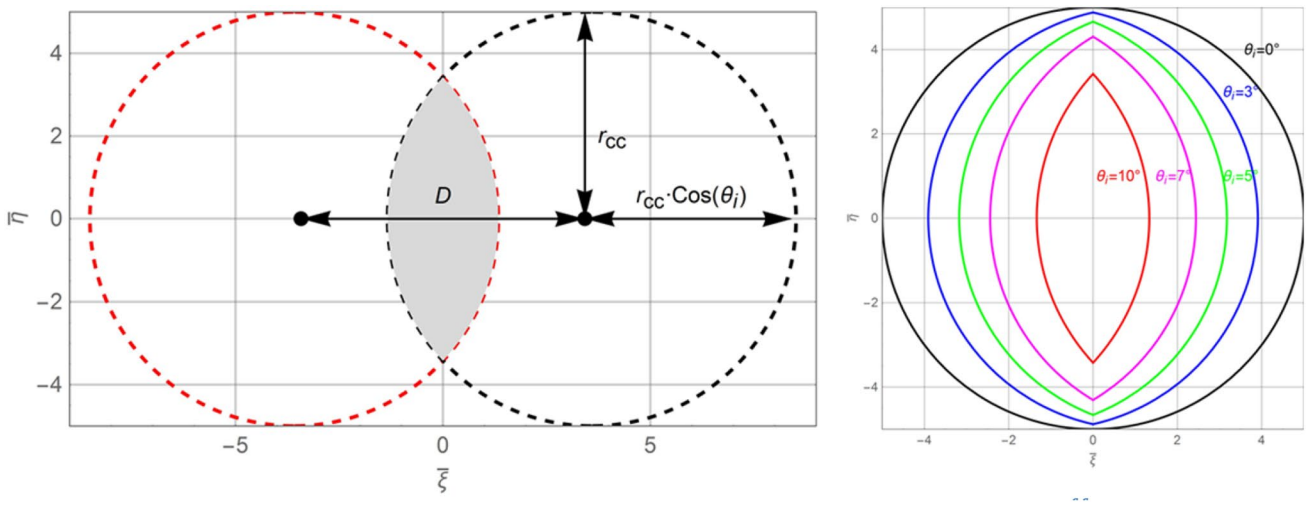


**Fig. 4** Left: demonstration of how to calculate the effective aperture shape  $\Omega$  and area  $A_{cc}^{eff}$  of the recessed retroreflector. Input (red dashed line) and output apertures (black dashed line) as drawn as seen by a laser beam incident on the recessed retroreflector. The apertures have the apparent shapes of an ellipse, which have a semi-major axes of  $r_{cc}$  along  $\bar{\xi}$  and a contracted semi-minor axis along  $\bar{\eta}$  of  $\cos \theta_i \cdot r_{cc}$ .

The overlap between the two apertures is the effective area  $A_{cc}^{eff}$  (gray colored area). The example is for an incidence angle of  $\theta_i = 10^\circ$ , a recession of  $R = 14$  mm and a CCR radius of  $r_{cc} = 5$  mm. Right: effective apertures for different incidence angles between  $\theta_i = 0^\circ$  and  $10^\circ$  as indicated in the figure

SLR stations, transmitter and receiver are located at the same position on earth. However, due to the velocity aberration the apparent receiver angle  $\theta_r$  takes the value  $\theta_r = \alpha$ , where  $\alpha$  is the velocity aberration, which depends on the satellite’s velocity. We further define the zenith angle of the satellite as  $\phi$ , and the incidence angle of the retroreflector as  $\theta_i$ .

**3.2 Calculation of the effective area**

As described in Sect. 2, the retroreflector has a circular entrance face with the visible radius  $r_{cc}$  and thus the effective area of the retroreflector at normal incidence ( $\theta_i = 0$ ) is given by

$$A_{cc} = \pi \cdot r_{cc}^2. \tag{1}$$

In this case, the shape of this aperture in Cartesian pupil-plane coordinates<sup>2</sup> ( $\bar{\xi}, \bar{\eta}$ ) is simply a circle, which can be described as:

$$\bar{\xi}(\bar{\eta}) = \pm \bar{F}(\bar{\eta}), \quad \text{where } |\bar{\eta}| \leq r_{cc},$$

$$\bar{F}(\bar{\eta})|_{\theta_i=0} = \sqrt{r_{cc}^2 - \bar{\eta}^2}. \tag{2}$$

For light rays at non-normal incidence the effective area as function of the incidence angle  $\theta_i$  can be derived from

<sup>2</sup> We follow the convention of Ref. [6] that  $\bar{\xi}$  and  $\bar{\eta}$  are Cartesian coordinates on the aperture of the retroreflector. Diffraction from this aperture leads to an intensity distribution at distance  $d$  (distance from the CCR to the SLR station) which is described by the coordinates  $\bar{x}$  and  $\bar{y}$ , where the  $\bar{\xi}$ -axes is parallel to the  $\bar{x}$ -axes.

calculating the overlap of “input” and “output” apertures as introduced in detail in Sect. 2.6 of Ref. [6].

A rotation of the retroreflector by the angle  $\theta_i$  along one axis (without loss of generality we choose a rotation along the  $\bar{\xi}$ -axis) will contract the apparent width of input and output apertures along the other direction by a factor of  $\cos \theta_i$ . This effectively turns the shape of the aperture as seen by the laser beam into the shape of intersecting ellipses (see left panel of Fig. 4). Note that the ellipses in Fig. 4 almost look like circles because the incidence angle  $\theta_i$  in the example is quite small ( $\theta_i = 10^\circ$ ).

Furthermore, input and output apertures of a recessed CCR are laterally displaced [5] by a distance  $D$  given by

$$D = 2(R \tan \theta_i + l \tan \theta'_i), \tag{3}$$

which depends on the CCR’s length  $l$ , as well as the recession  $R$  of the retroreflector.

Here,  $\theta'_i$  is the propagation angle inside the solid (n-BK7) retroreflector, which is related to the refractive index  $n$  and the incidence angle  $\theta_i$  via Snell’s law:

$$\theta'_i = \sin^{-1} \left( \frac{\sin \theta_i}{n} \right). \tag{4}$$

The shape of input and output apertures with these modifications are given by

$$\bar{F}(\bar{\eta}) = \cos \theta_i \cdot \left[ \pm (l \cdot \tan \theta'_i + R \cdot \tan \theta'_i) \mp \sqrt{r_{cc}^2 - \bar{\eta}^2} \right], \quad |\bar{\eta}| \leq \bar{\mu}, \tag{5}$$

where  $\bar{\mu}$  is given by

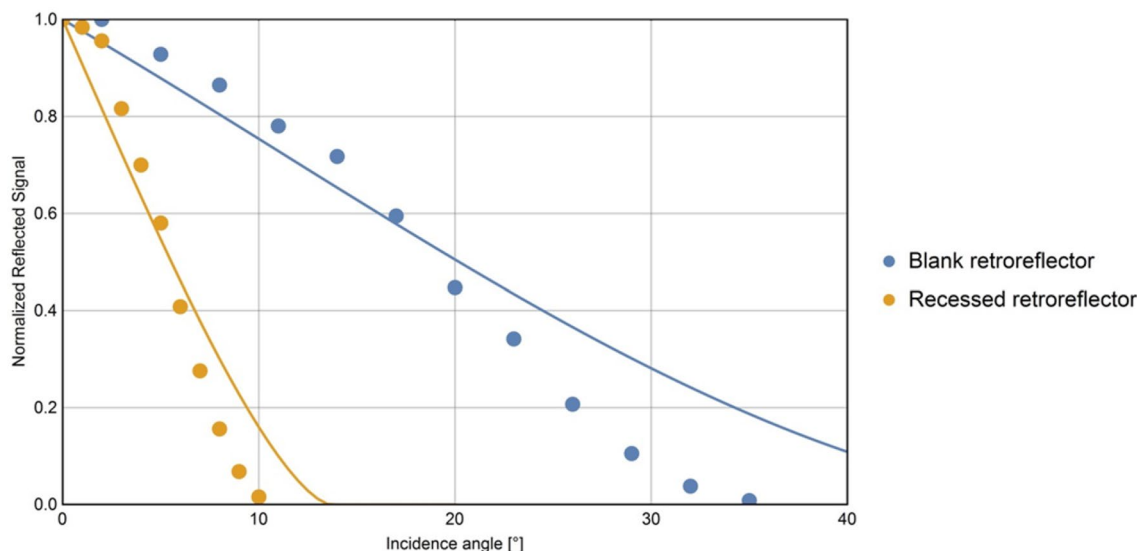


**Fig. 5** Measure, normalized reflectivity of the unmounted (blue dots), as well as the mounted, recessed CCR (yellow dots) as function of the incidence angle  $\theta_i$ . The solid lines represent the results of calculations

$$\bar{\mu} = r_{cc} \cdot \sqrt{1 - (l \cdot \tan \theta'_i + R \cdot \tan \theta_i)^2} \tag{6}$$

Finally, the effective aperture area  $A_{cc}^{eff}$  of the retroreflector is obtained by evaluating the overlap of input and output apertures (right panel of Fig. 4) via the integration:

$$A_{cc}^{eff} = \int_{\bar{\eta}=-\bar{\mu}}^{\bar{\mu}} \bar{\xi}(\bar{\eta})d\bar{\eta} = 4 \cdot \int_0^{\bar{\mu}} \bar{F}(\bar{\eta})d\bar{\eta} \tag{7}$$

### 3.3 Retroreflector reflectivity

When a laser with a homogeneous intensity distribution over the range of the aperture is incident on the retroreflector at an angle  $\theta_i$ , the reflected power should be proportional to the CCR’s effective area as calculated in Eq. (7).

In fact we built a simple optical setup to test the CCR’s normalized reflectivity as function of the incidence angle. Experimental details are given in Appendix A. For comparison, we did not only test the angular dependence of the recessed retroreflector ( $r_{cc} = 5$  mm,  $R = 14$  mm), but also for the unmounted CCR ( $r_{cc} = 6.35$  mm,  $R = 0$  mm).

Compared to the unmounted retroreflector, the reflectivity of the recessed CCR drops more rapidly when the CCR is tilted away from the normal incidence (the reflectivity of the unmounted CCR drops to 50% at  $\theta_i \approx \pm 20^\circ$ , whereas the reflectivity of the recessed CCR drops to 50% at  $\theta_i \approx \pm 5^\circ$ ).

Although the calculated and experimental reflectivity in Fig. 5 follow the same trends for both the blank and the recessed retroreflector, the agreement is not quite perfect. In particular, the measured reflectivity for the blank retroreflector

drops almost to zero at  $\theta_i \approx 35^\circ$ , whereas there should still be around 10% reflectivity according to our calculations. This might be caused by a combination of a slightly non-uniform beam profile (we used the center part of Gaussian HeNe laser expanded with a 20x beam expander, see Fig. 12), imperfections in the CCR manufacturing and possibly a slight offset in the orientation of the CCR along the axis perpendicular to  $\theta_i$ .

### 3.4 Far-field diffraction pattern

In order to estimate the intensity distribution reflected from the CCR to the earth, it is necessary to calculate and measure the FFDP of the recessed retroreflector.

As shown in Ref. [6] the optical cross section of a retroreflector illuminated by a uniform, coherent light ray across its aperture is given by

$$\sigma = 4\pi d^2 \rho \cdot U^2(\bar{x}, \bar{y}), \tag{8}$$

where  $d$  is the distance of the satellite from the SLR station,  $\rho$  is the CCR’s reflectivity at normal incidence and  $U(\bar{x}, \bar{y})$  is the electric field amplitude distribution from the retroreflector on a plane with coordinates  $(\bar{x}, \bar{y})$  at the distance  $d$ .

As the distance  $d$  is much larger than the retroreflector aperture, the FFDP can be calculated with the Fraunhofer approximation:

$$U(\bar{x}, \bar{y}) = \frac{1}{id\lambda} \cdot \exp\left\{i\frac{k}{2d}[2d^2 + (\bar{x}^2 + \bar{y}^2)]\right\} \iint_{\Omega} \exp\left[-i\frac{k}{d}(\bar{\xi}\bar{x} + \bar{\eta}\bar{y})\right]d\bar{\xi}d\bar{\eta}, \tag{9}$$

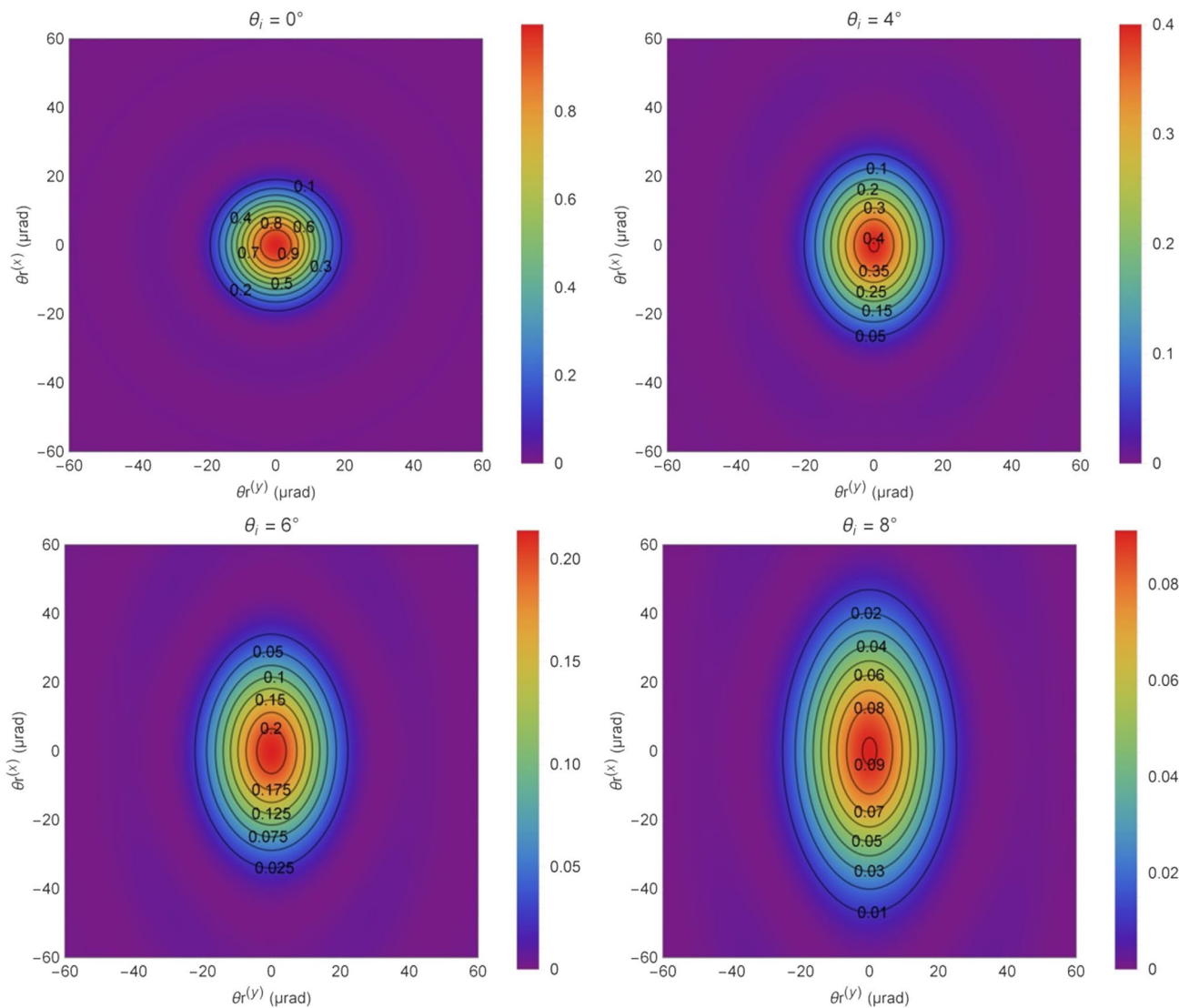


**Fig. 6** Calculated FFDP for the recessed retroreflector ( $R = 14$  mm,  $l = 10.16$  mm,  $r_{cc} = 5$  mm) for a wavelength of  $\lambda = 1064$  nm and four different incidence angles  $\theta_i$  between  $0^\circ$  and  $8^\circ$  as indicated above each panel

where  $k$  is the propagation number given by  $k = \frac{2\pi}{\lambda}$  and  $\Omega$  is the effective aperture, which strongly depends on the incidence angle  $\theta_i$  (see Fig. 4).

The diffraction integral can be solved numerically as described in the Appendix of Ref. [6]. Furthermore, we convert the FFDP from  $(\bar{x}, \bar{y})$  into a function of the receiver angles  $(\theta_r^{(x)}, \theta_r^{(y)})$  via

$$(\theta_r^{(x)}, \theta_r^{(y)}) = (\tan^{-1}(\bar{x}/d), \tan^{-1}(\bar{y}/d)). \quad (10)$$

Figure 6 shows the FFDP for the recessed retroreflector for different incidence angles  $\theta_i$  between  $0^\circ$  and  $7^\circ$ . For comparison, Fig. 7 provides experimental data for the FFDP obtained from measurements.

In accordance with the experimental results and the calculations, the FFDP at  $\theta_i = 0^\circ$  takes the shape of an Airy disk pattern, as expected for the diffraction from a circular aperture. When the retroreflector is tilted away from the normal, the overall reflected intensity drops (note that the different panels in the displayed FFDP have a different color scale) and the FFDP is broadened along the  $\theta_r^{(x)}$  axes (the retroreflector was tilted around an axis parallel to the  $y$ -axes).

The positive agreement between calculated and experimental FFDP patterns also shows that the manufacturing tolerance (especially the dihedral angles between the reflecting back faces of the retroreflector) is sufficient for the SLR experiment.

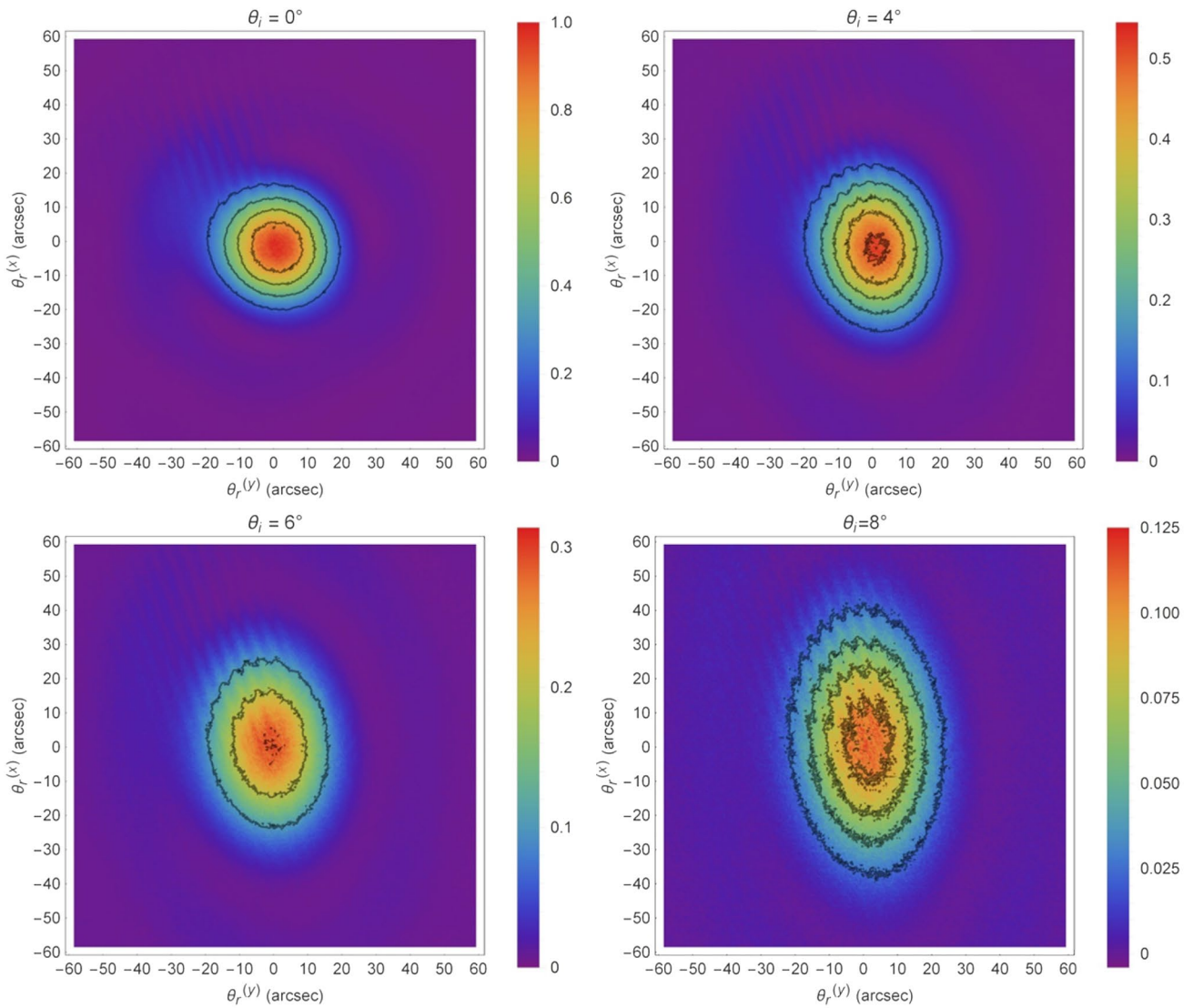


**Fig. 7** Measured FFDP of the flight module (recessed retroreflector). The FFDP was measured at 632 nm, but the axes are scaled to match a wavelength of  $\lambda = 1064$  nm. The different panels show data with the same incidence angles as those in Fig. 6

### 3.5 Velocity aberration

To obtain the retroreflector cross section as function of the incidence angle (Sect. 3.5) it is necessary to discuss the effect of the velocity aberration as the velocity aberration determines the apparent angles  $\theta_r^{(x)}$  and  $\theta_r^{(y)}$  of the SLR station and thus the intensity reflected in that direction.

The velocity aberration is given by [6, 7]

$$\alpha(h_S, \phi, \omega) = \alpha_m(h_S) \sqrt{\cos^2 \omega + \Gamma^2(h_S, \phi) \sin^2 \omega}, \tag{11}$$

where the maximum value  $\alpha_m$  is given by

$$\alpha_m(h_S) = \frac{2}{c} \sqrt{\frac{R_e^2 g}{R_e + h_S}}. \tag{12}$$

The contribution  $\Gamma^2(h_S, \phi)$  can be written as [6]:

$$\Gamma^2(h_S, \phi) = 1 - \left( \frac{R_e \sin \phi}{R_e + h_S} \right)^2, \tag{13}$$

where  $\phi$  is the zenith angle (see Fig. 3),  $R_e \approx 6371$  km is the radius of the earth,  $g \approx 9.81$  m/s<sup>2</sup> is the acceleration due to gravity,  $h_S$  is the height of the satellite above sea level and  $c$  is the speed of light.

The angle  $\omega$  depends on the satellite's movement with respect to the SLR station and is calculated from the unit vectors  $\hat{s}$  (direction from the center of the earth to the satellite),  $\hat{r}$  (direction from the SLR station to the satellite) and  $\hat{\nu}$  (direction of the satellites movement in space) [6]:

$$\omega = \cos^{-1}[(\hat{r} \times \hat{s}) \cdot \hat{v}]. \tag{14}$$

Thus, for a given height  $h_S$  and zenith angle  $\phi$ , the velocity aberration can take values in the range of

$$\begin{aligned} \alpha_{\max}(h_S) &= \alpha(h_S, \phi, \omega = 0) = \alpha_m(h_S) \\ \alpha_{\min}(h_S, \phi) &= \alpha(h_S, \phi, \omega = \pi/2) = \alpha_m(h_S)\Gamma(h_S, \phi), \end{aligned} \tag{15}$$

where  $\alpha_{\max}(h_S)$  and  $\alpha_{\min}(h_S, \phi)$  are the maximum and minimum values for the velocity aberration, respectively.

If we furthermore account for the rotation of the earth, these limits are slightly shifted to

$$\begin{aligned} \alpha_{\max}(h_S) &= \alpha_m(h_S) + \frac{2\bar{v}}{c} \\ \alpha_{\min}(h_S, \phi) &= \alpha_m(h_S)\Gamma(h_S, \phi) - \frac{2\bar{v}}{c}, \end{aligned} \tag{16}$$

where  $\bar{v}$  is the velocity of the SLR station:

$$\bar{v} = \frac{2\pi R_e \cos \varphi}{T_{\text{day}}}, \tag{17}$$

which depends on the stations latitude ( $\varphi$ ), and the duration of 1 day ( $T_{\text{day}}$ ).

Figure 8 shows these limits for the velocity aberration as function of the zenith angle  $\phi$  as calculated for a satellite on a circular orbit of height  $h_S = 600$  km (estimated height of the CUBE<sub>L</sub> satellite) when ranged with the DLR SLR station ( $\varphi \approx 48.78^\circ$ ). The maximum velocity aberration is 10.81 arcsec independent of the zenith angle, while the minimum velocity aberration varies from 9.97 arcsec at  $\phi = 0^\circ$  (satellite is in zenith over the SLR station) to 7.01 arcsec at  $\phi = 70^\circ$ .

### 3.6 Retroreflector cross section as function of incidence angle and velocity aberration

Figure 9 shows the normalized retroreflector cross section as function of the incidence angle  $\theta_i$  and the velocity aberration  $\alpha$  for a wavelength of 1064 nm (as used by the DLR SLR station at the Uhlandshöhe).

If the retroreflector is tilted along an axis perpendicular to the projected relative satellite velocity:

$$\mathbf{v}' = [\mathbf{v} - (\mathbf{v} \cdot \hat{r})\hat{r}], \tag{18}$$

the direction of the SLR station is given by the apparent angles of  $\theta_r^{(x)} = 0$  and  $\theta_r^{(y)} = \alpha$  (compare Fig. 6). This situation is presented in panel a of Fig. 9. In the plotted range, the maximum cross section (shown as red line) for a given velocity aberration is always found at  $\theta_i = 0^\circ$ . At higher incidence angles the cross section drops rapidly, see panel b.

Panels c and d of Fig. 9 describe the situation when the retroreflector is tilted in the direction of the relative satellite velocity ( $\theta_r^{(x)} = \alpha$  and  $\theta_r^{(y)} = 0$ ). Here, we also find that the

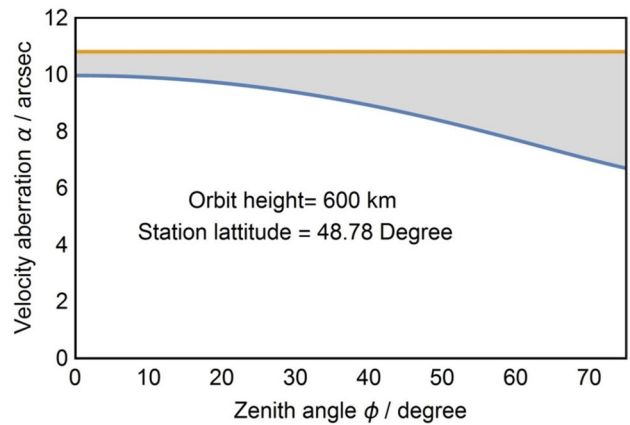


**Fig. 8** Calculation of minimum (blue solid line) and maximum (yellow solid line) values for the velocity aberration as function of the zenith angle  $\phi$  for a circular satellite orbit at a height of 600 km above sea level and a station latitude of  $48.78^\circ$  (Uhlandshöhe Research Observatory). At each zenith angle the exact value of the velocity aberration depends on the satellites orbit, but can only take values from the gray area in-between these limits

cross section peaks at  $\theta_i = 0^\circ$  for velocity aberrations in the range of 7.01 to 10.81 arcsec and then rapidly falls off with a full width at half maximum smaller than  $\theta_i = \pm 5^\circ$ . This is very beneficial for verifying the satellites attitude via satellite laser ranging. In this situation the relative signal strength returned from the CCR is directly correlated to the error of the satellites attitude control operating in station pointing mode targeting the SLR station.

It is important to note that the CCR cross section as a function of the incidence angle depends on the laser wavelength. In fact, most other SLR stations operate at 532 nm. In this case, the broadening due to diffraction is weaker and the cross section as function of the incidence angle can also feature two distinct maxima, see bottom right panel of Fig. 10.

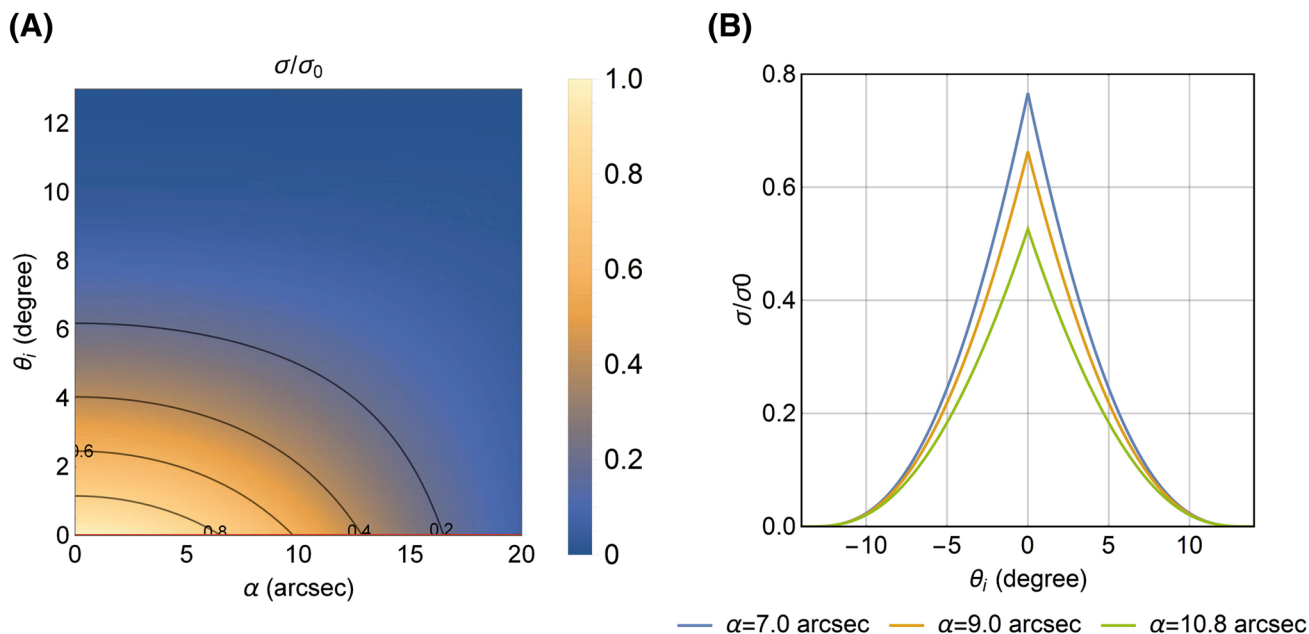
### 4 Feasibility of testing the attitude control system Via SLR

To estimate the number of detected photo electrons per sent laser pulse  $\eta_p$  during satellite laser ranging with the DLR SLR station “Uhlandshöhe Research Observatory” the radar link equation is employed given by [6, 8]

$$\eta_p = \frac{E_T \lambda}{hc} \eta_t \frac{G_T}{4\pi d^2} \frac{\sigma_0}{4\pi d^2} \frac{\sigma}{\sigma_0} A_r \eta_r \eta_q T_a^2 T_c^2. \tag{19}$$

Assuming a circular satellite orbit with a height of  $h_S = 600$  km, the distance from the satellite to the SLR station  $d$  (neglecting the station height above sea level) is correlated to the zenith angle  $\phi$  via

### CCR rotated perpendicular to $v'$



### CCR rotated in the direction of $v'$

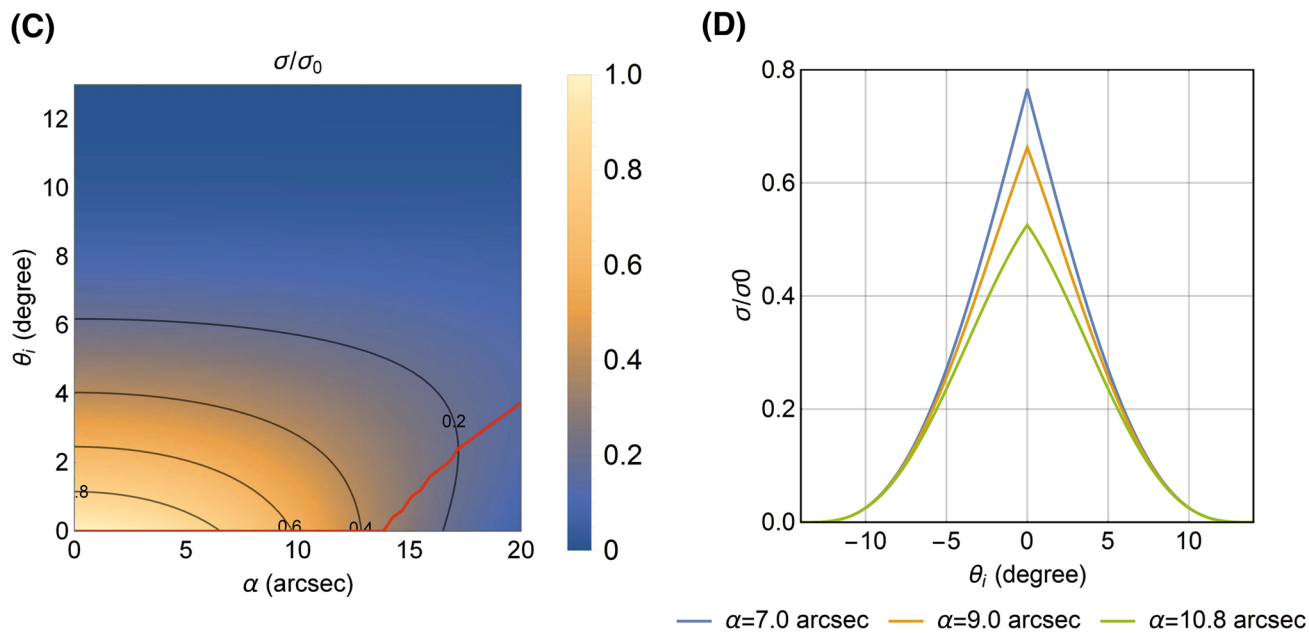
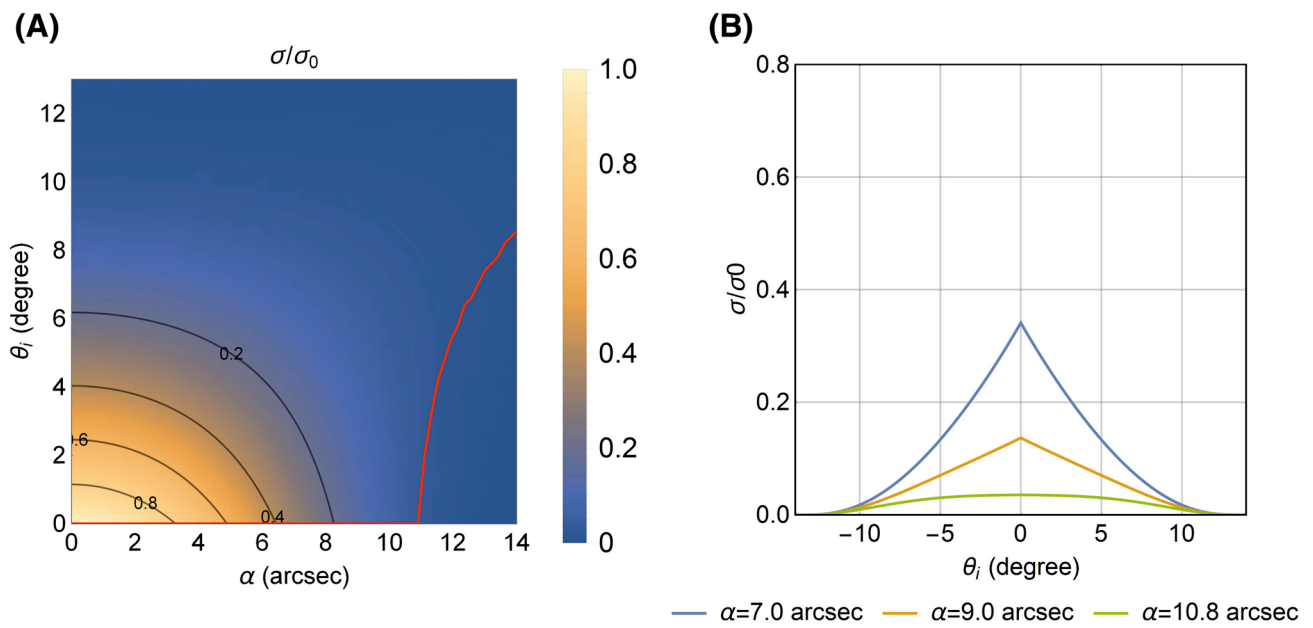


**Fig. 9** Normalized retroreflector cross section as function of the incidence angle  $\theta_i$  and velocity aberration  $\alpha$  for SLR at a wavelength of 1064 nm. The different panels are described in the text. The CCR cross section peaks at  $\theta_i = 0^\circ$  for all relevant velocity aberrations,

which is beneficial for an attitude verification via SLR. The red lines in **a** and **c** show the angle  $\theta_i$  with a maximum reflected intensity for each velocity aberration  $\alpha$

## CCR rotated perpendicular to $\mathbf{v}'$



## CCR rotated in the direction of $\mathbf{v}'$

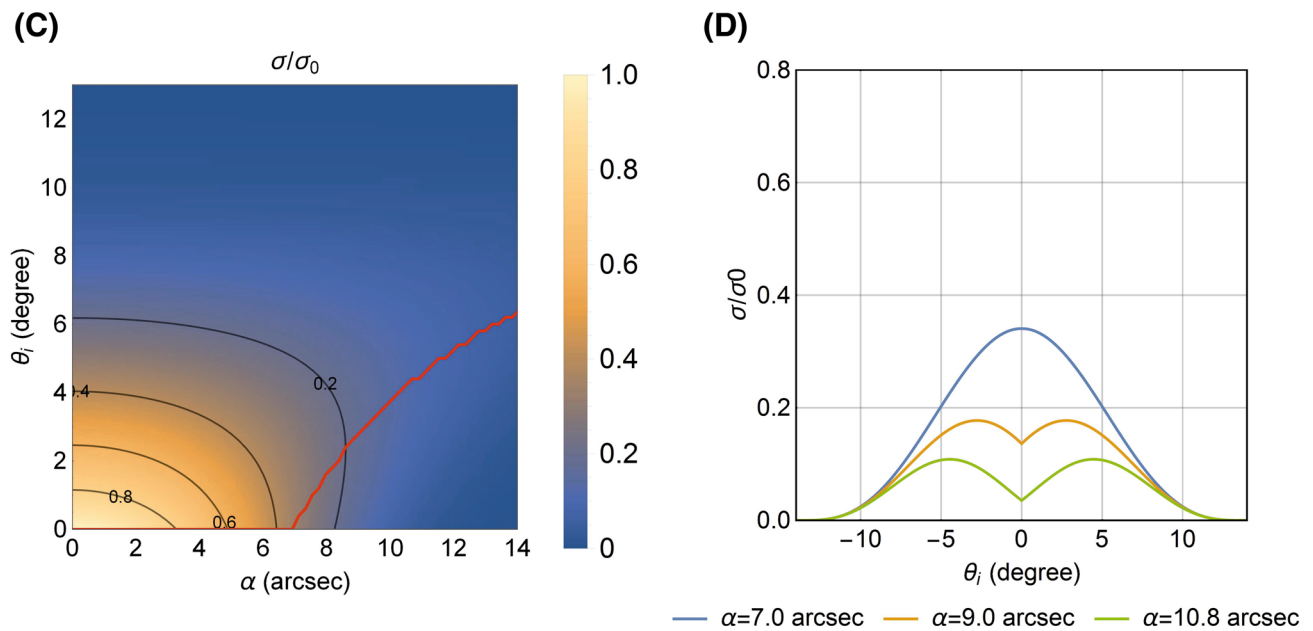


**Fig. 10** Same as Fig. 9, but for a wavelength of 532 nm. The CCR cross section peaks at  $\theta_i \neq 0^\circ$ , depending on the velocity aberration, which makes an attitude verification via SLR more complicated

**Table 2** Parameters used for photon budget calculations with the radar link equation

Parameter	Value	Information
$E_T$	20 $\mu$ J	Laser pulse energy (in front of the transmitter)
$\lambda$	1064 nm	Wavelength
$\eta_t$	0.25	Efficiency of transmitter (using an optical fiber)
$G_T$	$\frac{8}{\theta_i^2} \exp\left[-2\left(\frac{\theta}{\theta_i}\right)\right] = 1.2 \times 10^8/\text{rad}^2$	Transmitter gain for a Gaussian beam, where $\theta_i$ is the beam divergence (half angle between the beam center and the $1/\exp(1)^2$ intensity point) estimated to 200 $\mu$ rad $\theta$ is the beam pointing error estimated to half the beam divergence ( $\frac{\theta}{\theta_i} = 0.5$ )
$\sigma_0$	$\rho \frac{4\pi}{\lambda^2} (\pi r_{CC}^2) = 5.48 \times 10^4 \text{ m}^2$	CCR cross section at normal incidence and without velocity aberration, $\rho = 0.8$ (reflectivity of retroreflector) $r_{CC} = 5$ mm (radius of retroreflector aperture)
$\sigma/\sigma_0$	value between 0..1	Correction factor accounting for the CCR cross section as function of incidence angle and velocity aberration (see Fig. 9)
$A_r$	$\pi \times (0.2 \text{ m})^2 = 0.13 \text{ m}^2$	Area of receiving optics
$\eta_r$	0.5	Efficiency of receiving optics
$\eta_q$	0.3	Efficiency of detector (photo multiplier tube)
$T_a$	0.8	Atmospheric transmission (estimated)
$T_c$	0.8	Cirrus-cloud transmission (estimated)

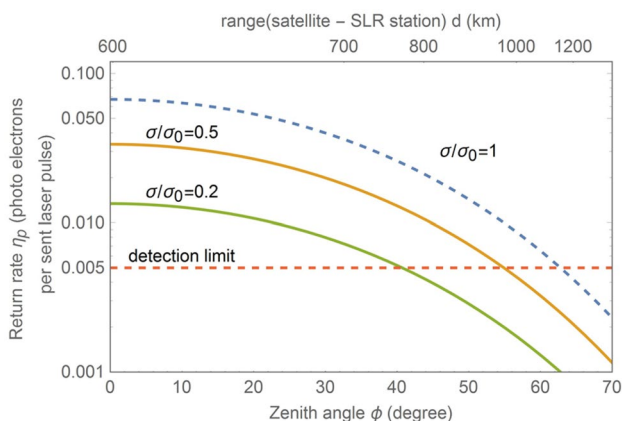


**Fig. 11** Calculated return rate  $\eta_p$  for SLR of the recessed CCR for a satellite on a circular orbit at a height of 600 km as function of the incidence angle  $\phi$  as explained in the text. The calculation was performed for the SLR station Uhlandshöhe Research Observatory

$$d = \sqrt{R_e^2 \cos^2 \phi + 2R_e h_S + h_S^2} - R_e \cos \phi. \tag{20}$$

All other parameters used for the photon budget calculations are summarized in Table 2.

Figure 11 shows the calculated number of detected photo electrons per sent laser pulse  $\eta_p$  as function of the zenith angle  $\phi$ . The return rate depends on the normalized retroreflector cross section ( $\sigma/\sigma_0$ ). For the CCR design and  $\lambda = 1064$  nm,  $\sigma/\sigma_0$  takes values between  $\geq 0.5$  at normal incidence ( $\theta_i = 0^\circ$ ) and  $\approx 0.2$  for a tilted retroreflector (at an

incidence angle of  $\theta_i = \pm 5^\circ$ , see Fig. 9). For these cases, the calculated return rates are presented as yellow and green lines, respectively. The detection limit, which allows for a reliable tracking of the satellite, depends on the laser pulse repetition rate. With the current design, a number of detected photo electrons per sent laser pulse of  $\eta_p = 0.05$  is a conservative estimate for this limit (red, dashed line in Fig. 11).

We find that for a satellite pointing to the DLR SLR station, ranging of CUBEL should be possible at zenith angles  $\phi$  smaller than  $55^\circ$ . For  $\phi < 40^\circ$  it should be possible to track the satellite even at an incidence angle of  $\theta_i = \pm 5^\circ$ . In this regime it should also be possible to test the CubeSat’s attitude control by commanding the CubeSat to change its attitude with respect to  $\theta_i$ , while simultaneously observing the signal strength in satellite laser ranging. As the signal drops off sharply with  $\theta_i$ , it is reasonable to assume, that the pointing accuracy of the satellite can be determined to within  $\pm 2^\circ$ .

The exact design of such an experiment needs to be developed in future work. A first guess would be to repeatedly rotate the satellite in such a way that  $\theta_i$  (deviation from station pointing mode) changes at a rate of  $\sim 1^\circ/\text{s}$  around a range of  $\pm 5^\circ$ . This would mean that a “peak” return signal (corresponding to  $\theta_i = 0^\circ$  for SLR at 1064 nm) for the rotation around one axis could be found within 10 s. This time is fortunately much shorter than the expected link duration, which is estimated to be in the order of several minutes (depending on the exact orbit over the SLR station).

## 5 Conclusion and outlook

We designed a recessed retroreflector which will be launched to space on the CubeSat CUBE<sub>L</sub>. The design is based on a commercially available, 12.7 mm diameter CCR mounted into a specifically designed titanium holder that recesses the CCR's entrance face. In order to select a CCR with a high optical and manufacturing quality, FFDPs of eight retroreflectors were measured and the best retroreflector was selected as a flight module. We believe that the recessed CCR assembly, which is a lightweight and small design optimized for use on a CubeSat, should allow for a coarse verification of the attitude control to within  $\pm 2^\circ$ .

The retroreflector was designed for a specific CubeSat mission with the goal of advancing laser communication technology. Nonetheless, we hope that the detailed discussion of the experimental and mathematical effort involved in the project and described in this publication will enhance the use of recessed CCRs' in the largely growing CubeSat market.

**Acknowledgements** The authors thank the DLR Bremen (Institute of Space Systems) for performing vibration tests, our industrial partner Tesat-Spacecom, the satellite integrator Gomspace and the mechanical workshop at DLR Stuttgart for constructing and manufacturing the titanium SLR mount (Institute of Technical Physics). Furthermore, the authors thank Dr. Ludwig Grunwaldt (GFZ Potsdam) for very helpful discussions during the project.

**Open Access** This article is distributed under the terms of the Creative Commons Attribution 4.0 International License (<http://creativecommons.org/licenses/by/4.0/>), which permits unrestricted use, distribution, and reproduction in any medium, provided you give appropriate credit to the original author(s) and the source, provide a link to the Creative Commons license, and indicate if changes were made.

## Appendix A: Experimental details for the measurement of the CCR reflectivity and far field diffraction pattern

Figure 12 shows a schematic of the experimental setup used to measure the FFDP and the CCR reflectivity at DLR Stuttgart. A helium neon laser (Polytec GmbH) is expanded by a factor of 20 with a combination of  $f = -25$  mm and  $f = 500$  mm lenses. To avoid unwanted reflections, the beam is cropped by an aperture (not shown in Fig. 12) with a diameter of 16 mm to provide a laser

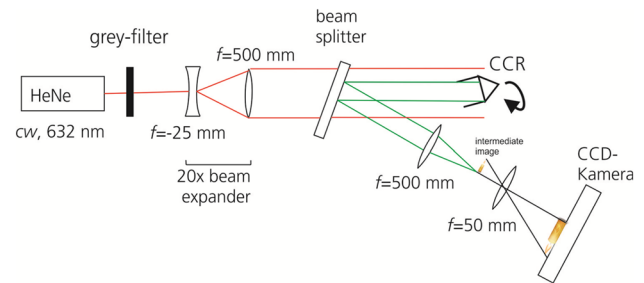


**Fig. 12** Schematic of the measurement of the CCR reflectivity far-field diffraction pattern

beam with a diameter larger than the entrance face of the retroreflector ( $2r_{cc} = 10$  mm).

The beam then passes through a 50% transmission beam splitter and illuminates the CCR. During the experiment, the CCR can be either mounted as a blank retroreflector or together with its recessing mount. Furthermore the CCR is can be rotated by an arbitrary angle  $\theta_i$ . Retro-reflected light from the CCR then encounters the beam splitter for a second time and is focused by an  $f = 500$  mm lens. At the position of the focus, the reflected power can be measured with an energy detector. Alternatively, the beam profile in the focus (which corresponds to the far-field image) can be imaged on a CCD camera with an  $f = 50$  mm lens.

To convert pixels in the FFDP's to scattering angles (in arcsec) the CCR was replaced by a circular aperture (3.1 mm in diameter) in front of a reflective mirror. This generates an Airy disk and the intensity minima can be used for calibration.

## Appendix B: Experimental details for the measurement of the far-field diffraction pattern at GFZ Potsdam

Measurements of the PPDP and the selection of the best retroreflector for use as a flight module on the Cube<sub>L</sub> satellite were done at GFZ Potsdam and the experimental setup has been described previously [9]. The CCR #7 (FFDP highlighted with a red frame in (Fig. 13) was selected as flight retro, because of its symmetric FFDP.

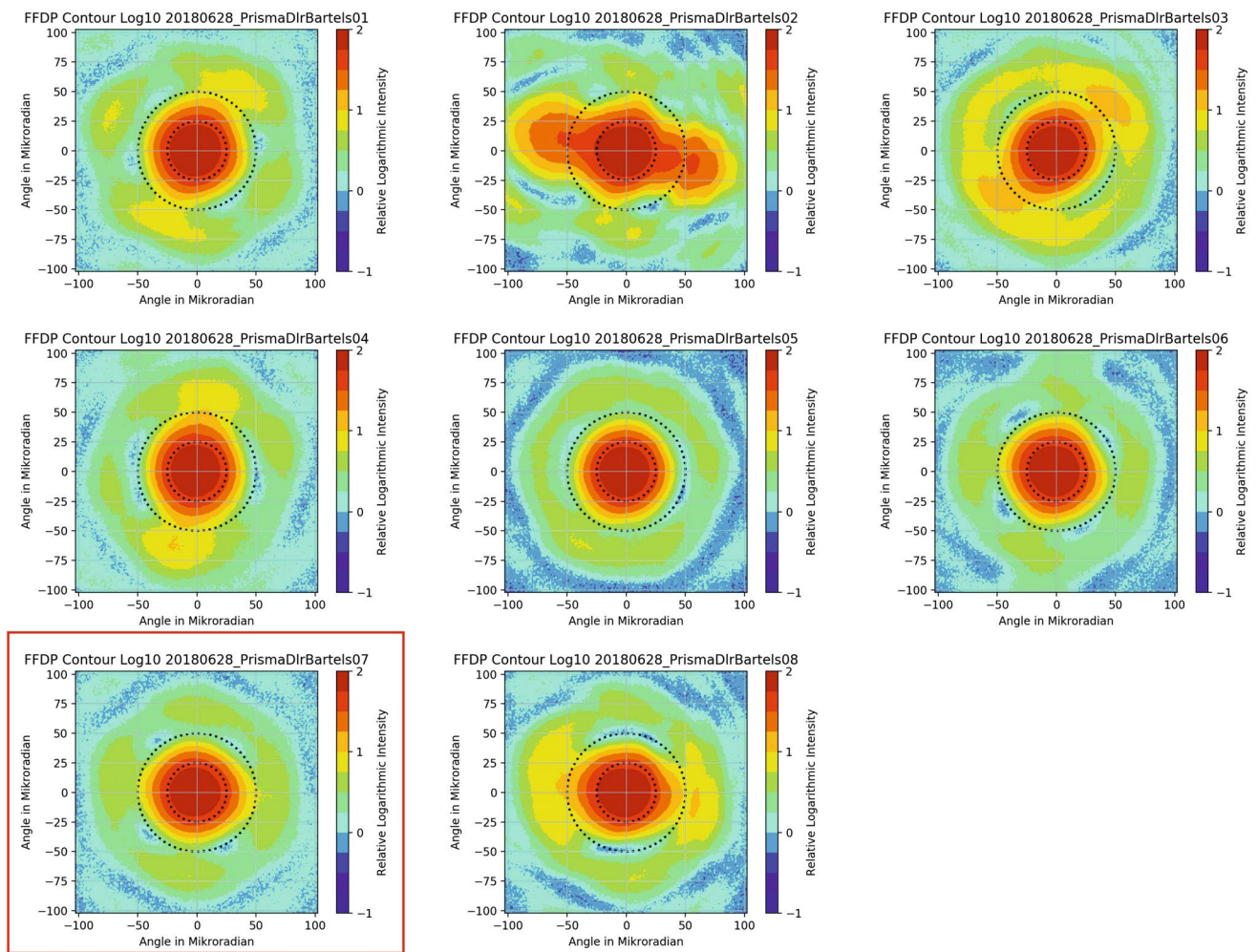


**Fig. 13** Logarithmic plot of the FFDP of several CCR's of the same batch as measured at a wavelength of  $\lambda=532$  nm at normal incidence. The CCR #7 (FFDP highlighted with a red frame) was selected as flight retro and will be send to space as part of the CUBEL satellite

## References

- Schmidt, C., Fuchs, C.: The OSIRIS program at DLR. In: Proceedings of SPIE, Free-space laser communication and atmospheric propagation, vol. 10524, pp. 10524 (2018). <https://doi.org/10.1117/12.2290726>
- Flying Laptop. <https://directory.eoportal.org/web/eoportal/satellite-missions/f/flying-laptop> (2018). Accessed 18 June 2019
- Hampf, D., et al.: First successful satellite laser ranging with a fibre-based transmitter. *Adv. Space Res.* **58**(4), 498–504 (2016)
- Humbert, L., et al.: Innovative laser ranging station for orbit determination of LEO objects with a fiber-based laser transmitter. *CEAS Space J.* **8**(4), 59–63 (2015). <https://doi.org/10.1007/s12567-015-0106-0>
- Arnold, D.A.: Method of calculating retroreflector-array transfer functions. SAO Special Report No. 382, pp 165 (1979)
- Stephenson, P.C.L.: Satellite laser ranging photon-budget calculations for a single satellite cornercube retroreflector: attitude control tolerance. National Security and ISR Division, DST-Group-TR-3172 (2015)
- Degnan, J.: A tutorial on retroreflectors and arrays for SLR. In: ILRS Workshop, Frascati, Italy (2012)
- Degnan, J.J.: Millimeter accuracy satellite laser ranging: a review. In: Smith, D.E., Turcotte, D.L. (eds.) Contributions of Space Geodesy to Geodynamics: Technology, pp. 133–162. American Geophysical Union (AGU) (2013). <https://doi.org/10.1029/gd025p0133>
- Grunwaldt, L., Neubert, R., Barschke, M.F.: Optical tests of a large number of small COTS cubes. In: Presented at the 20th International Workshop on Laser Ranging (2016)

**Publisher's Note** Springer Nature remains neutral with regard to jurisdictional claims in published maps and institutional affiliations.